SOLAR SMALL-SCALE MAGNETOCONVECTION

R. F. STEIN

Department of Physics and Astronomy, Michigan State University, East Lansing, MI 48823; stein@pa.msu.edu

AND

Å. NORDLUND

Niels Bohr Institute, Juliane Maries Vej 30, Dk-2100 Copenhagen Ø, Denmark; aake@astro.ku.dk

ABSTRACT

Magnetoconvection simulations on mesogranule and granule scales near the solar surface are used to study the effect of convective motions on magnetic fields: the sweeping of magnetic flux into downflow lanes, the twisting of magnetic field lines, and the emergence and disappearance of magnetic flux tubes. From weak seed fields, convective motions produce highly intermittent magnetic fields in the intergranular lanes that collect over the boundaries of the underlying mesogranular scale cells. Instances of both emerging magnetic flux loops and magnetic flux disappearing from the surface occur in the simulations. We show an example of a flux tube collapsing to kilogauss field strength and a case of flux disappearance due to submergence of the flux. We note that observed Stokes profiles of small magnetic structures are severely distorted by telescope diffraction and seeing, so caution is needed in interpreting low-resolution vector magnetograms of small-scale magnetic structures.

Subject headings: MHD — Sun: granulation — Sun: magnetic fields

1. INTRODUCTION

Magnetic field plays a crucial role in the structuring and heating of the solar outer atmosphere: the chromosphere, corona, and heliosphere. Convective motions drive the solar dynamo, and together with differential rotation, meridional circulation and the tachocline shear layer produce emergent magnetic flux on scales from active region complexes down to the intergranular lanes. We have simulated magnetoconvection and dynamo action on mesogranule and granule scales in the upper layers of the convection zone. Our objectives are to understand the processes of flux emergence, "flux tube" formation, flux disappearance and dynamo action near the solar surface and to clarify the interpretation of observations by relating what is observable to what is occurring in the simulations.

Convection is inherently three-dimensional, nonlinear, and nonlocal. As a result, most progress in understanding convection has come from analyzing numerical simulations. Two complementary approaches using numerical simulations have both contributed toward understanding convection. One uses simplified physics to explore the basic properties of convection and its parameter space variations (e.g., Hurlburt & Toomre 1988; Cattaneo et al. 1991; Nordlund et al. 1992; Hurlburt et al. 1996, 2002; Brummell et al. 1998; Weiss et al. 1996; Tao et al. 1998; Tobias et al. 1998, 2001; Porter & Woodward 2000; Thelen & Cattaneo 2000; Emonet & Cattaneo 2001; Cattaneo et al. 2003; Cline et al. 2003; Brun et al. 2004; Bushby & Houghton 2005). The other uses realistic solar physics to enable quantitative comparisons with solar observations and explore physical processes in the solar convection zone (e.g., Nordlund 1985; Freytag et al. 1996; Stein & Nordlund 1998, 2001; Rosenthal et al. 1999; Steiner et al. 1998; Asplund et al. 2000; Leka & Steiner 2001; Keller et al. 2004; Carlsson et al. 2004; Vögler et al. 2005; Khomenko et al. 2005). Here we report on some magnetoconvection simulations of this latter type.

We find that the magnetic field is very intermittent, with a stretched exponential distribution. The field lines are swept into the turbulent downflow lanes and plumes by the diverging, ascending broad plumes of warm fluid and become very tangled (e.g., Steiner et al. 1998; Weiss et al. 1996, 2002). In a stratified atmosphere with scale height and horizontal cell size increasing with depth, the field is swept to the boundaries of the larger underlying cells. "Flux tubes" emerging through the surface are produced either from emerging loops that then open up through the top boundary or by concentration of magnetic flux by horizontal flows in the intergranular lanes. These "flux tubes" do not exist far below the surface where their field lines connect to many different locations and other surface "flux tubes." We also find instances in which emerging loops get pulled back down below the surface by convective motions.

We first briefly describe the simulation in § 2 and then present our results in §§ 3–8. Next we present some comparisons with solar observations in § 9 and finally discuss some of the implications and directions for future work.

2. THE SIMULATION

Magnetoconvection near the solar surface is modeled by performing realistic simulations (Stein & Nordlund 2000) of magnetoconvection in a small domain 6×6 Mm on a side, extending from the temperature minimum 0.5 Mm above continuum optical depth unity to 2.5 Mm below the visible surface using a grid $253 \times 253 \times 163$ grid points. This gives a horizontal resolution of 25 km and a vertical resolution of 15 km near the surface increasing to 35 km at depth. The equations we solve are conservation of mass,

$$\frac{\partial \ln \rho}{\partial t} = -\boldsymbol{u} \cdot \nabla \ln \rho - \nabla \cdot \boldsymbol{u}, \qquad (1)$$

conservation of momentum,

$$\frac{\partial \boldsymbol{u}}{\partial t} = -\boldsymbol{u} \cdot \nabla \boldsymbol{u} + \boldsymbol{g} - \frac{P}{\rho} \nabla \ln P + \frac{1}{\rho} \boldsymbol{J} \times \boldsymbol{B} + \frac{1}{\rho} \nabla \cdot \tau, \quad (2)$$
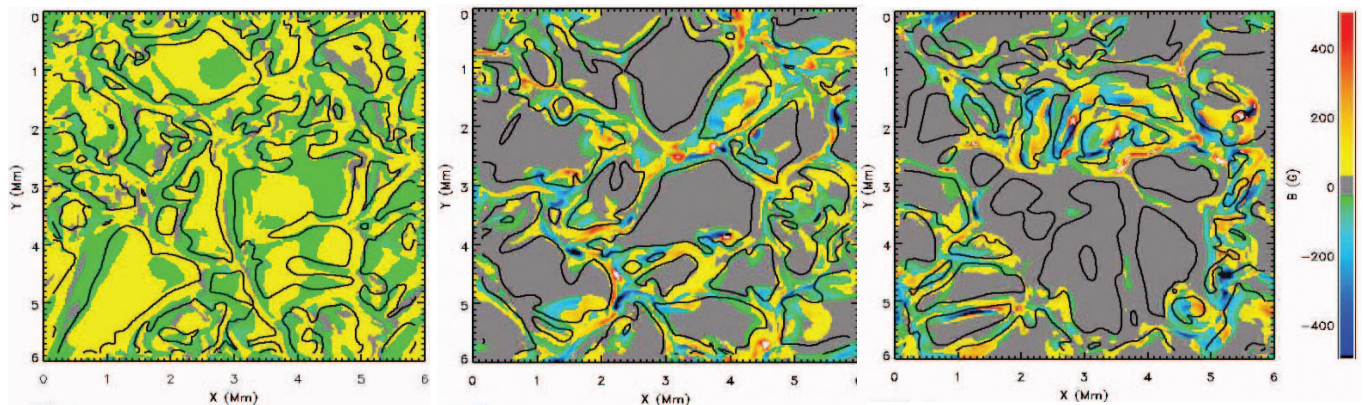
FIG. 1.—Surface magnetic field strength after half a minute (*left*), after 10 minutes (*center*), and after 30 minutes (*right*). Black contours are zero-velocity contours, which outline the granules. Fields stronger than 0.5 kG appear as white and black. Field magnitudes less than 30 G are shown in gray. Initially the entire surface is covered with 30 G horizontal field. Diverging upflows first sweep the granules clear of strong fields and on a longer timescale sweep the interiors of mesogranules free of strong fields.

conservation of energy,

$$\frac{\partial e}{\partial t} = -\boldsymbol{u} \cdot \nabla e - \frac{P}{\rho} \nabla \cdot \boldsymbol{u} + Q_{\mathrm{rad}} + Q_{\mathrm{visc}} + Q_{\mathrm{Joule}}, \quad (3)$$

and the induction equation for the vector potential,

$$\frac{\partial \boldsymbol{A}}{\partial t} = \boldsymbol{u} \times \boldsymbol{B} - \eta \boldsymbol{J}. \quad (4)$$

Here ρ is the density, $\boldsymbol{u}$ is the velocity, P is the pressure, e is the energy per unit mass, $\boldsymbol{A}$ is the vector potential, $\boldsymbol{B}$ is the magnetic field, $\boldsymbol{J}$ is the current, τ is the viscous stress tensor, η is the resistivity, and Q_{rad}, Q_{visc}, and Q_{Joule} are the radiative, viscous, and Joule heating, respectively. All variables are centered at the same locations—the cell centers.

Rotation and Coriolis forces are neglected, because on this small scale of mesogranulation, with a depth of only 2.5 Mm, the flows do not feel the rotation.

To achieve high accuracy with small numerical damping we use high-order derivatives. The horizontal spatial derivatives are calculated using sixth-order compact centered finite differences (Lele 1992) and the vertical derivatives are third-order, calculated from spline fits to the functions. Time advance is by a third-order predictor corrector (Hyman 1979). The code is stabilized by a hyperviscosity that removes short-wavelength noise without damping the longer wavelengths (Stein & Nordlund 1998).

Boundary conditions control how the fluid behaves in accordance with the conservation laws. The boundaries of our computational domain are "virtual boundaries." The region we simulate is, in reality, coupled to an external medium, about which we have little a priori information. However, convection is driven by entropy fluctuations generated near the surface by radiative cooling. Deeper layers asymptotically approach an adiabatic mean state, in which ascending gas is nearly isentropic and uniform. For this reason, the lack of information about the region below our model is not likely to be a significant source of uncertainty. The region above our model contains too little mass to be able to significantly influence the interior. To minimize the effects of the boundaries, we use periodic horizontal boundary conditions and transmitting top and bottom boundary conditions. To peg conditions at their solar values we specify the entropy of the incoming fluid at the bottom. For stability, the total pressure

(gas plus magnetic) is made horizontally uniform by adjusting the mass and energy densities consistent with isentropy. The magnetic field tends toward a potential field at the top and at the bottom horizontal magnetic flux is advected into the computational domain by inflows and in outflows the field is constrained to have $\partial B_x/\partial z = \partial B_y/\partial z = \partial^2 B_z/\partial z^2 = 0$ (see the Appendix for details). There is a net Poynting flux into the domain at the bottom that increases linearly with time, reaching 0.5% of the solar flux by the end of the run. There is also a net Poynting flux into the domain at the top, but because the field tends toward a potential field there, it is much smaller, of order 0.007% of the solar flux, and does not vary significantly with time.

It is important that the lower boundary conditions do not prevent magnetic energy from being advected out of the domain. Imposing, for example, a vertical field condition there would force the Poynting flux to vanish at the boundary, and prevent magnetic energy and flux from leaving the domain. As discussed in more detail below, the magnetic field has a strong tendency to be swept into the downdrafts near the surface as the flow overturns, and thus advection out of the domain is presumably a dominant magnetic energy loss mechanism, which is important to include when studying dynamo action in the surface layers.

Ionization is significant in the energy balance of the upper convection zone, where about 2/3 of the energy is transported in the form of ionization energy. This gets dumped into the radiation field at the surface when hydrogen becomes neutral. In order to obtain solar values for the temperature and velocity fluctuations, we use a realistic tabular equation of state calculated from the Uppsala atmospheres package (Gustafsson et al. 1975), which includes LTE ionization and excitation of hydrogen, helium, and other abundant atoms plus formation of H_2 molecules.

Radiative energy exchange is critical in determining the structure of the upper convection zone. The interaction between convection and radiation near the surface determines what we observe and escaping radiation cools the plasma that reaches the surface, which produces the low-entropy fluid whose buoyancy work drives the convection. Since the top of the convection zone occurs near the level where the continuum optical depth is one, neither the optically thin nor the diffusion approximations give reasonable results. We solve the three-dimensional, LTE, nongray radiation transfer in our model. The radiative energy exchange rate is found by formal solution of the Feautrier equations along straight rays, here one vertical and four slanted rays, which are rotated in azimuth 15° each time step in order effectively probe all the
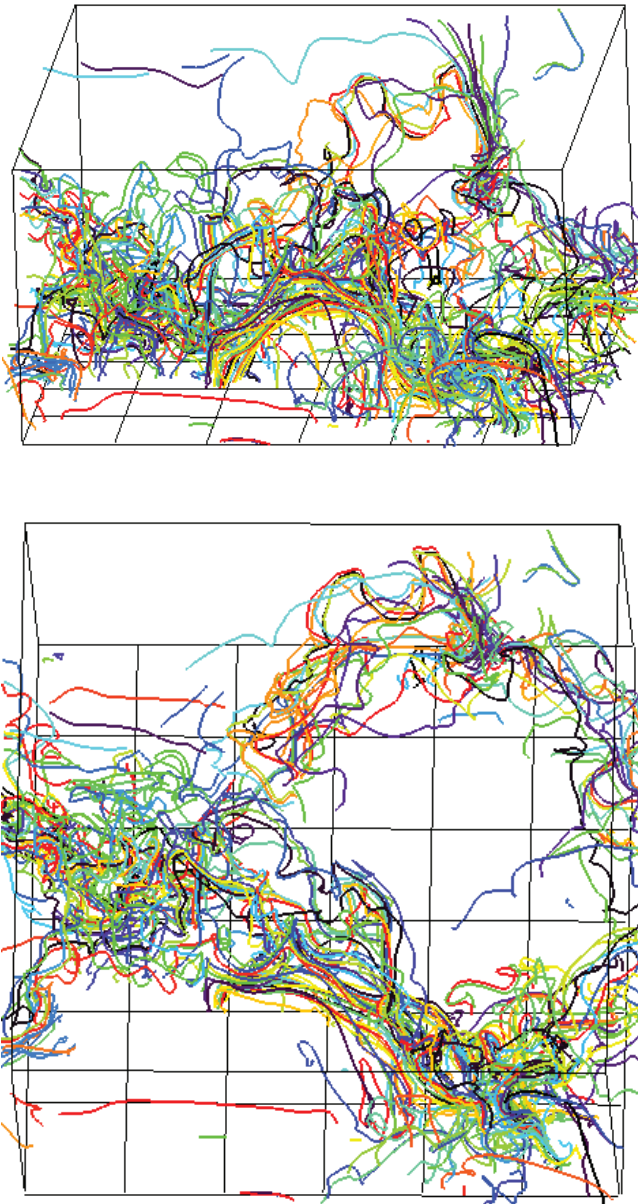
FIG. 2.—Magnetic field lines in a snapshot viewed from an angle (*top panel*) and from the top (*bottom panel*). Boxes at the bottom are 1×1 Mm. Horizontal magnetic field is advected into the computational domain through the bottom boundary by upflows in the interiors of mesogranules (*red field line near the bottom left and in the top view also top left*). It is swept out of the granules and mesogranules into the downflows in the mesogranule boundaries. It also gets concentrated, stretched, and twisted by the convective motions. When a flux loop opens up through the top boundary it can leave behind one leg as a "flux tube" (*top right of the angle view*).

surrounding medium. The opacity and source function are interpolated to the location of the intersections of the rays with each horizontal plane. The continuous opacities are calculated from the Uppsala atmospheres package (Gustafsson et al. 1975) with UV opacities enhanced according to the prescription of Magain (1983) and line opacities are determined from the Uppsala ODF tables (Gustafsson et al. 1975). The calculation is enormously sped up by drastically reducing the number of wavelengths at which we solve the Feautrier equations. We make the simplifying approximation of grouping the opacity at each wavelength into 4 bins according to its magnitude corresponding to the continuum, weak, medium, and strong lines (Nordlund 1982;
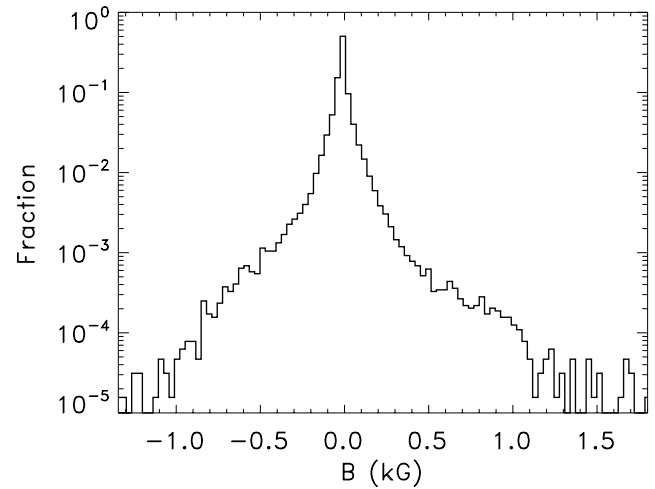

FIG. 3.—Histogram of magnetic field strength at $\tau = 1$ for the 30 G case. It has a stretched exponential shape.

Skartlien et al. 2000; Stein & Nordlund 2003). The consequence of this grouping of opacities is that all wavelengths in a given bin have optical depth unity at approximately the same geometrical depth so that integrals over optical depth commute with the sum over wavelengths. The source function for each bin is the weighted sum of the Planck functions, at each table temperature, over all the wavelengths in the bin.

The calculations were started from a snapshot of relaxed hydrodynamic solar convection on which was imposed a uniform horizontal 1 or 30 G seed field. During the course of the simulation the magnetic field is concentrated and stretched by the turbulent convective flow. Magnetic flux escapes through the top and bottom boundaries and new horizontal magnetic flux is advected into the computational box by fluid ascending through the bottom of the domain. To date we have run a 2 hr sequence with the 1 G initial field and a 1 hr sequence with the 30 G initial field.

3. FLUX EXPULSION

These simulations started with an infinite scale uniform horizontal field (Fig. 1*a* at 30 s). The diverging granular upflows sweep the field into the downflow intergranular lanes on a granular timescale ($\sim$8 minutes) (Fig. 1*b*). On a longer timescale of mesogranulation ($\sim$30 minutes) the field gets swept to the boundaries of the underlying mesogranules (Fig. 1*c*) by the diverging upflows on these larger scales. The field is concentrated by horizontal flows along the downflow lanes surrounding the granules and mesogranules as well as twisted and stretched by the turbulence in the downflows (Fig. 2). Inside the granules there is some very weak field, but strong fields occur primarily in the intergranular lanes that correspond to the mesogranular boundaries. On the Sun, the magnetic field is also swept to the magnetic network on the boundaries of the supergranules in times of a few hours. Why isn't a larger scale magnetic pattern seen on the Sun? Probably because the speed of horizontal flows decreases with increasing horizontal scale, so that there is not enough time to produce a larger pattern from flux that is continually emerging on small scales of granules and mesogranules and reconnecting and submerging in the network.

4. FIELD-LINE MORPHOLOGY

Figure 2 shows selected magnetic field lines for one snapshot from the 30 G case. At the bottom is seen the horizontal magnetic
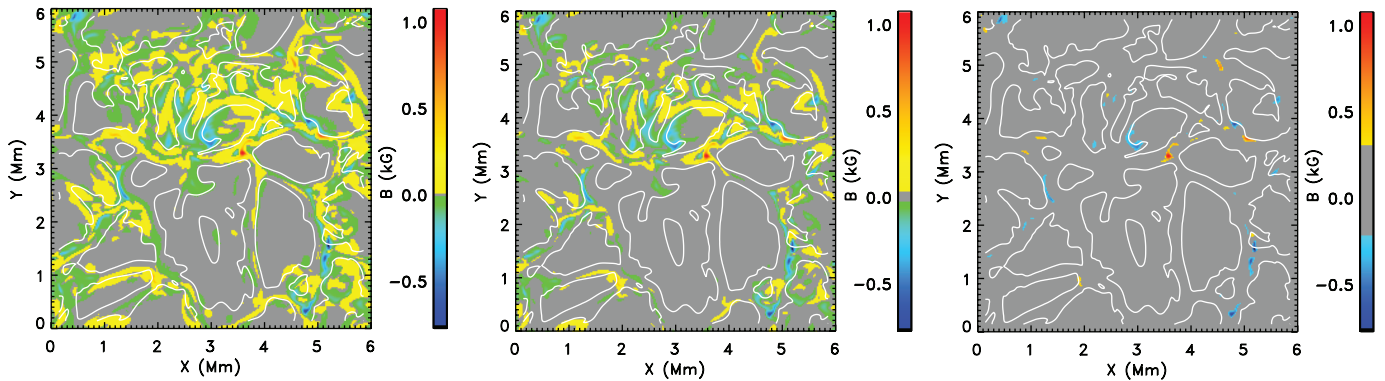
Fig. 4.—Image of magnetic field at $\tau = 1$ with superimposed zero velocity contours to outline the granules, for the case of a 30 G uniform horizontal seed field. From left to right, field magnitudes less than 3, 30, and 300 G, respectively, are shown in gray. The magnetic field is concentrated into the intergranular lanes. It is highly intermittent, with strong fields occupying a tiny fraction of the total area.

field being advected into the computational domain by ascending fluid in the center of mesogranules, as shown by the red 1–3 Mm long nearly horizontal field lines near the bottom of the box. Higher up are the twisted field lines produced by the turbulent convective motions. It looks pretty chaotic. However, the field is actually organized by the underlying mesogranules as can be seen by looking at the same field lines from the top (Fig. 2). The entering horizontal field is seen to be located in the interiors of the mesogranules where the upflows occur. The overlying chaotic magnetic field has been swept out of the granules and mesogranules by diverging upflows. It is advected into the boundaries of the mesogranules, where it is twisted and stretched by the turbulent descending plasma (e.g., Stein & Nordlund 2000, Fig. 13). The vortical downdrafts produce highly twisted field lines in the mesogranule boundary downflows seen in Figure 2. Although there is a lot of small-scale structure and loops, note that the field lines are connected over long distances. This is due partly to the initial state of infinitely long field lines whose influence is not yet completely removed. It is also due to the smaller scale magnetic flux advected in by the mesogranular upflows being stretched to much greater size by the diverging nature of these upflows.

5. MAGNETIC FIELD CONCENTRATION AND ENHANCEMENT

The diverging upflows together with horizontal flows along intergranular lanes toward their vertices and turbulent downflows produce a highly intermittent field with a stretched exponential distribution of field strengths (Fig. 3). Similar results have been found in the Boussinesq calculations of Thelen & Cattaneo (2000) and Emonet & Cattaneo (2001) and are observed for the solar magnetic field by, for example, Harvey & White (1999) and Hagenaar (2001). A stretched exponential distribution means that the stronger the field the smaller the fraction of the area it occupies. Fields of 3 G fill all the intergranular lanes and exist even inside some of the granules. Fields stronger than 30 G have been swept out of the granules into the intergranular lanes and even some the intergranular lanes have no field stronger than 30 G. Finally, fields stronger than 300 G occur hardly anywhere in the domain (Fig. 4).

6. MAGNETIC LOOP EMERGENCE

In these simulations, flux emerges through the surface, merges, fragments, cancels, and submerges. Figure 5 is a sequence of images of the signed surface magnetic field at 10 s intervals showing a flux loop emerging on the right-hand side and its foot points separating (black and white indicate strong oppositely directed vertical components). New flux emerges sometimes inside granules, sometimes at their edges, and sometimes in intergranular lanes. Flux emerging inside granules is quickly swept into intergranular lanes by the diverging granular upflows.

Figure 6 is a sequence of three-dimensional images of magnetic field magnitude showing a rising loop emerging through the surface. The loop rises up through the surface, and its legs, where they pass through the visible surface, initially separate with time. As the loop rises through the photosphere the magnitude of the field decreases as the loop spreads out.

7. MAGNETIC "FLUX TUBES"

Magnetic "flux tubes" sticking up through the surface form by two processes: First, magnetic loops that emerge through the surface and then open out (to space) through the upper boundary
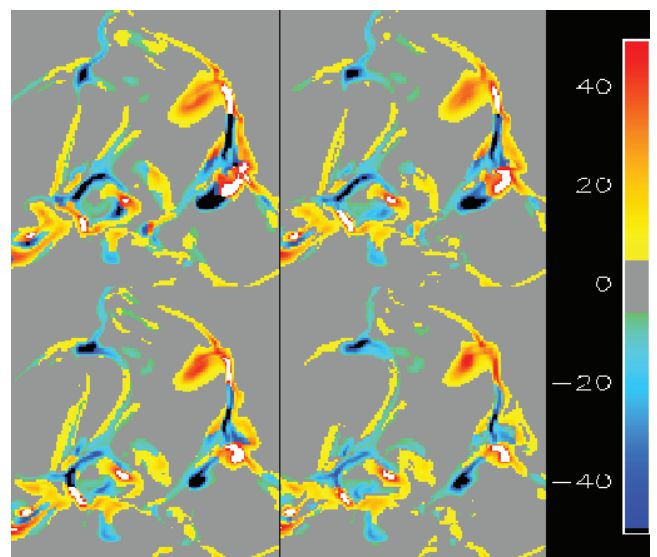

Fig. 5.—Four snapshots of the surface magnetic field magnitude (with the sign of the vertical component), for the 1 G horizontal inflow field case, at 10 s intervals (TL, TR, BL, BR), showing the emergence and footpoint separation of a magnetic loop on the right-hand side and the disappearance of magnetic flux on the left-hand side. The color scale at the right is in gauss.
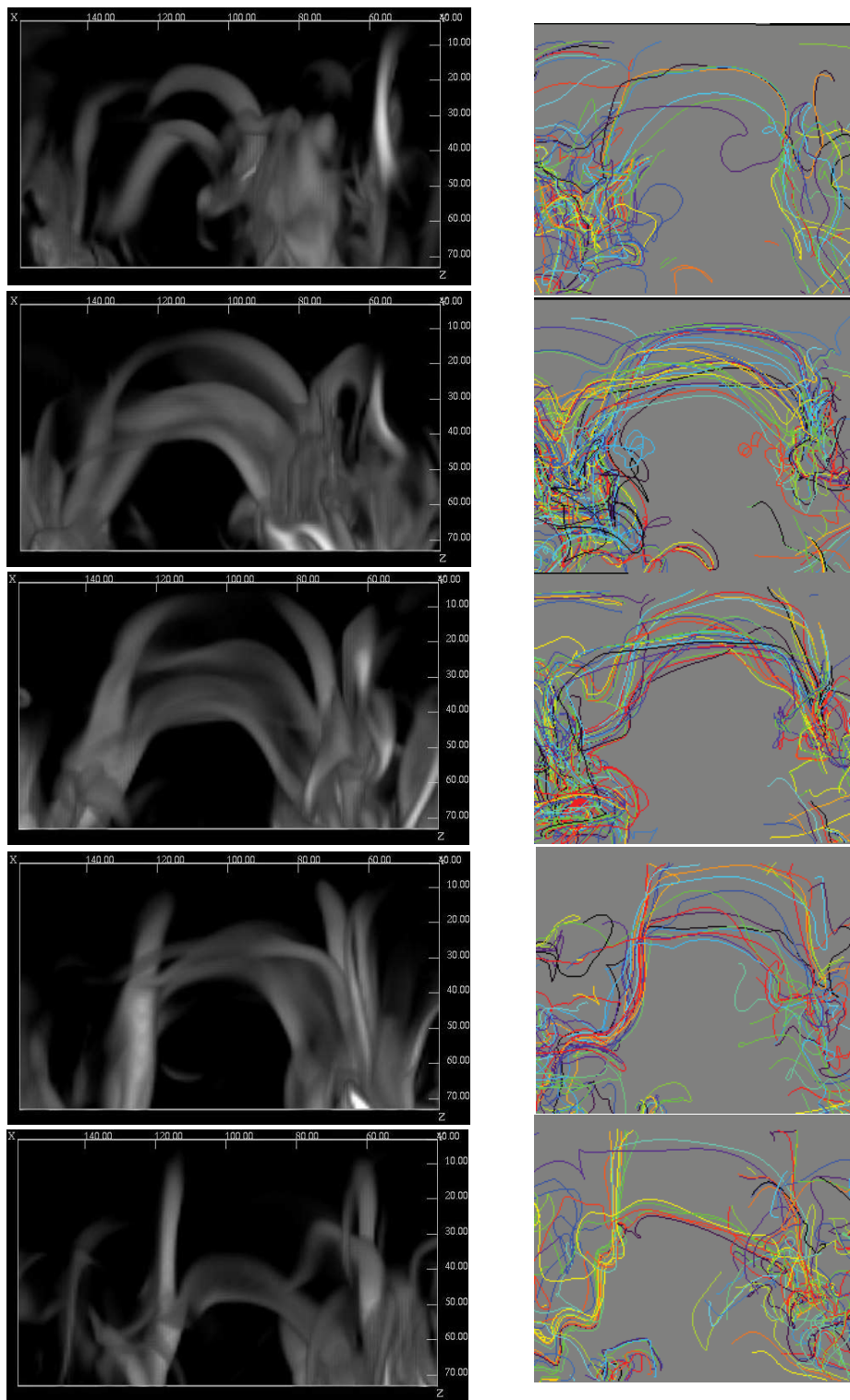
Fɪɢ. 6.—Magnitude (*left*) and field lines (*right*) of magnetic field at 1 minute intervals, showing the emergence of a magnetic loop and its opening out through the upper boundary to leave behind a "flux tube." A second loop is pulled back down in the last frame. The horizontal width of the images is 2.8 Mm. The vertical extent is 1.0 Mm for the field magnitude and 1.5 Mm for the field lines. (The numbers are the grid indices.) Note: field lines are not the same from snapshot to snapshot.
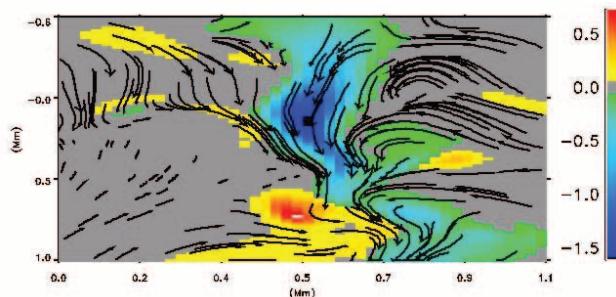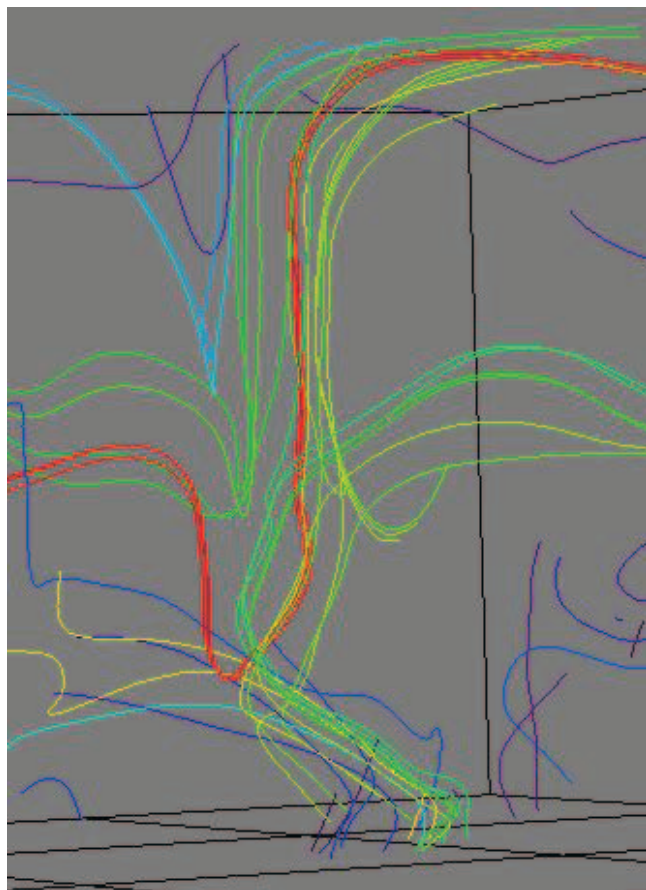
Fig. 7.—(*a*) Magnetic field lines through a 1.5 kG "flux tube" that forms and gets partially evacuated in the 30 G simulation. Near the surface the magnetic field lines form a flux tube bundle. Below the surface the field lines diverge in several different directions. (*b*) Image of "flux tube" vertical magnetic field with fluid velocity vectors in the *x-z* plane. The color scale is the vertical field strength in kG. The tube is in the process of being evacuated by downflowing fluid. The density is less than its surroundings at and above the surface but greater than its surroundings below the surface.

leave one or both of their legs behind as an isolated "flux tube." Second, horizontal flows in the intergranular lanes (see Stein & Nordlund 1998) advect weak, nearly vertical field and concentrate it at the vertices of granular and mesogranular downflow lanes.

The first process is illustrated in the sequence of snapshots of magnetic field lines (Fig. 6). Sometimes one leg of the rising loop remains compact and becomes a "flux tube" as the loop opens out through the upper boundary, while the other leg becomes spread out and does not become a "flux tube". Note that the bundle of field lines forming the "flux tube" remains coherent down to a depth of about 1 Mm, and then the field lines connect to many different regions.

The second process is the occasional concentration of magnetic flux, by horizontal flows in the intergranular lanes, to form a "flux tube" at the vertices of the lanes (Fig. 7). The "flux tube" is cooler than its surroundings and is being evacuated by downflows that are strongest at its periphery, leading into the vertex. Near the surface and above, the density inside the "flux tube" is already less than its surroundings, but at greater depth the density is still higher than its surroundings, where it is decreasing as the cooler plasma inside the magnetic concentration settles downward.

However, it is unclear how relevant the concept of an isolated "flux tube" is for the weak, incoherent magnetic fields in the quiet Sun. As illustrated by Figure 7, the coherent bundle of

field lines composing the flux tube at the surface is connected to many different locations, with a complex topology, below the surface. In addition, as seen in Figure 2 the field lines that form the individual loops and "flux tubes" can actually be connected over large distances and go in and out of several loops and hence participate in more than one "flux tube." *Transition Region and Coronal Explorer* (*TRACE*) observations show that also above the surface field lines from a "flux tube" connect to many different end points. Finally, as also seen in Figure 2, below the surface the weak field lines are twisted and tangled by the convective motions and do not form anything looking like a "flux tube" on a fine scale.

8. FLUX DISAPPEARANCE

Instances of magnetic flux disappearing from the surface also occur in the simulations. Figure 5 also shows, on the left side, oppositely (vertical component) directed flux that comes together and partially disappears. In this case the flux disappearance is due to submergence of the magnetic loop. Figure 8 shows a sequence of horizontal slices at heights from 5 to 125 km above the mean visible surface (*columns*) and at 10 s intervals (*rows*). At the lower left there is initially a small bipole visible at all heights with red and blue indicating oppositely directed loop legs. Note that the loop legs are farther apart at lower altitude. As time goes on the bipole disappears from the higher elevations and the legs that were initially well separated at the lower
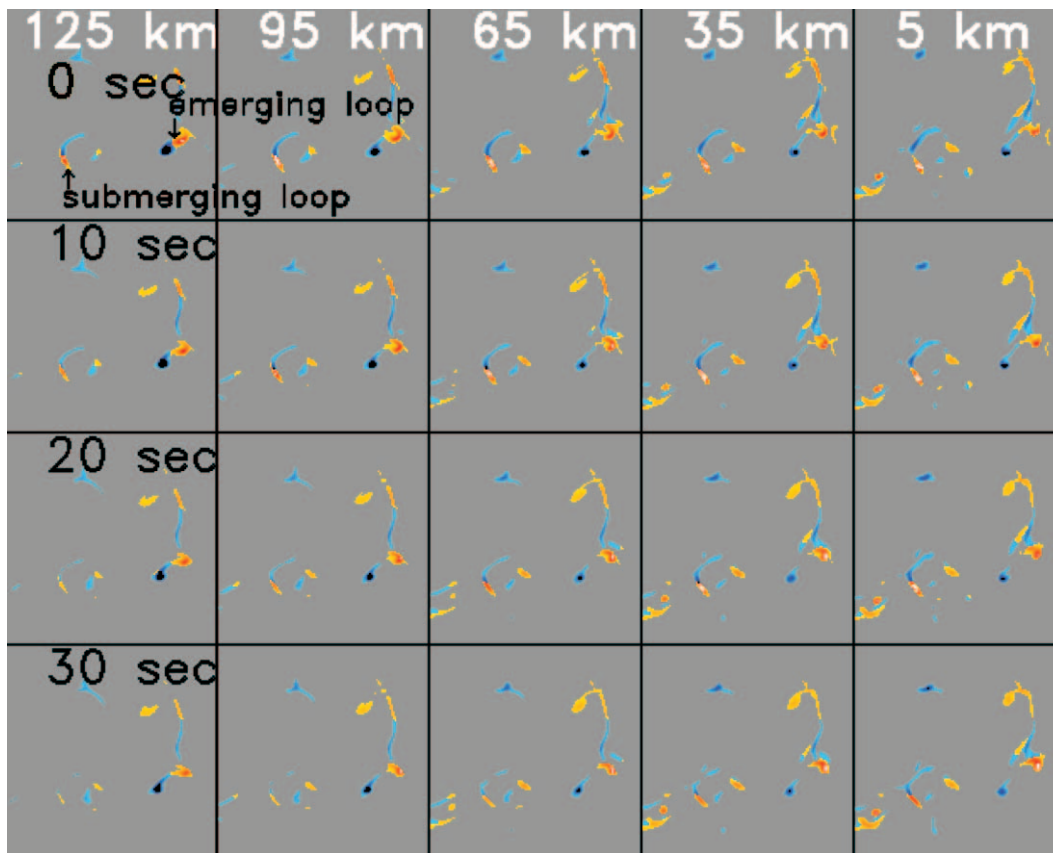
FIG. 8.—Horizontal slices of magnetic field strength at 10 s intervals (*rows*) at 30 km height separation (*columns*) above the mean visible surface. Red and yellow have opposite polarity to blue. Gray is weak field. At the right of each image is an emerging bipole whose legs separated with decreasing height and increasing time. At the left is a submerging bipole whose legs approach with increasing time and which disappears at higher elevations at later times.

elevations come together, showing that this magnetic loop is submerging.

9. COMPARISON WITH OBSERVATIONS

How is what one observes related to what is actually happening on the Sun? Stokes profiles are used to determine the vector magnetic field at the solar surface. Figure 9 shows the stokes profiles for Fe ɪ6302 as would be observed by the 97 cm Swedish Solar Telescope on La Palma with perfect seeing (*thick lines*). The light gray lines show the profiles from the 9 individual 25 km² pixels covering a 75 × 75 km region around the central point. The profile as it would be observed is calculated by convolving the Airy function for the Swedish 1 m Solar Telescope with the Stokes profiles for the individual simulated grid locations. The observed profile amplitudes are significantly degraded from what would be seen with infinite resolution. Observers should take this as a warning in interpreting their measured profiles (cf. Khomenko et al. 2005). Another consequence of telescope and atmospheric seeing is that the morphology of the observed field may be dramatically altered, so that for small flux concentrations one observes roundish flux tubes, whereas the actual field distribution follows the intergranular lanes and where it collects at lane vertices and looks like an amoeba (Fig. 10).

Resolution thus has a tremendous impact on how one interprets observations. At low resolution (even with the old 47 cm Swedish Solar Telescope on La Palma), magnetograms show objects that look like round flux tubes (Fig. 10, *left image*). The new telescope with twice the diameter reveals a much more complex structure (*center image*), while the simulations show that the actual situation is even more complex (*right image*). Hence, high-resolution observations are crucial for learning the actual solar magnetic field structure.

10. SUMMARY

Diverging convective upflows sweep the magnetic field to the boundaries of granules, mesogranules and on still longer timescales supergranules. Turbulent convective downdrafts stretch and twist any seed magnetic field enhancing magnitude. Near the solar surface the field reaches pressure balance with the surrounding plasma (about 1.5 kG). As a result of these processes the field is very intermittent, having a stretched exponential distribution in magnitude.

Magnetic loops of varying lengths emerge through the surface and open outward in the low-density atmosphere leaving their legs behind as "flux tubes." Flux concentrations also form by the shuffling of magnetic field by horizontal flows toward vertices in the intergranular lanes. Magnetic flux disappears from the surface when magnetic loops get pulled down by the convective motions or when field lines with different orientations are brought together by the convective motions and reconnection occurs.

Limited resolution in observations of Stokes profiles results in degraded average profiles and as a result a significant fraction of small-scale magnetic flux is missed. It is important therefore to use comparisons of observations with high-resolution simulations to determine the true magnetic field strengths and fluxes.
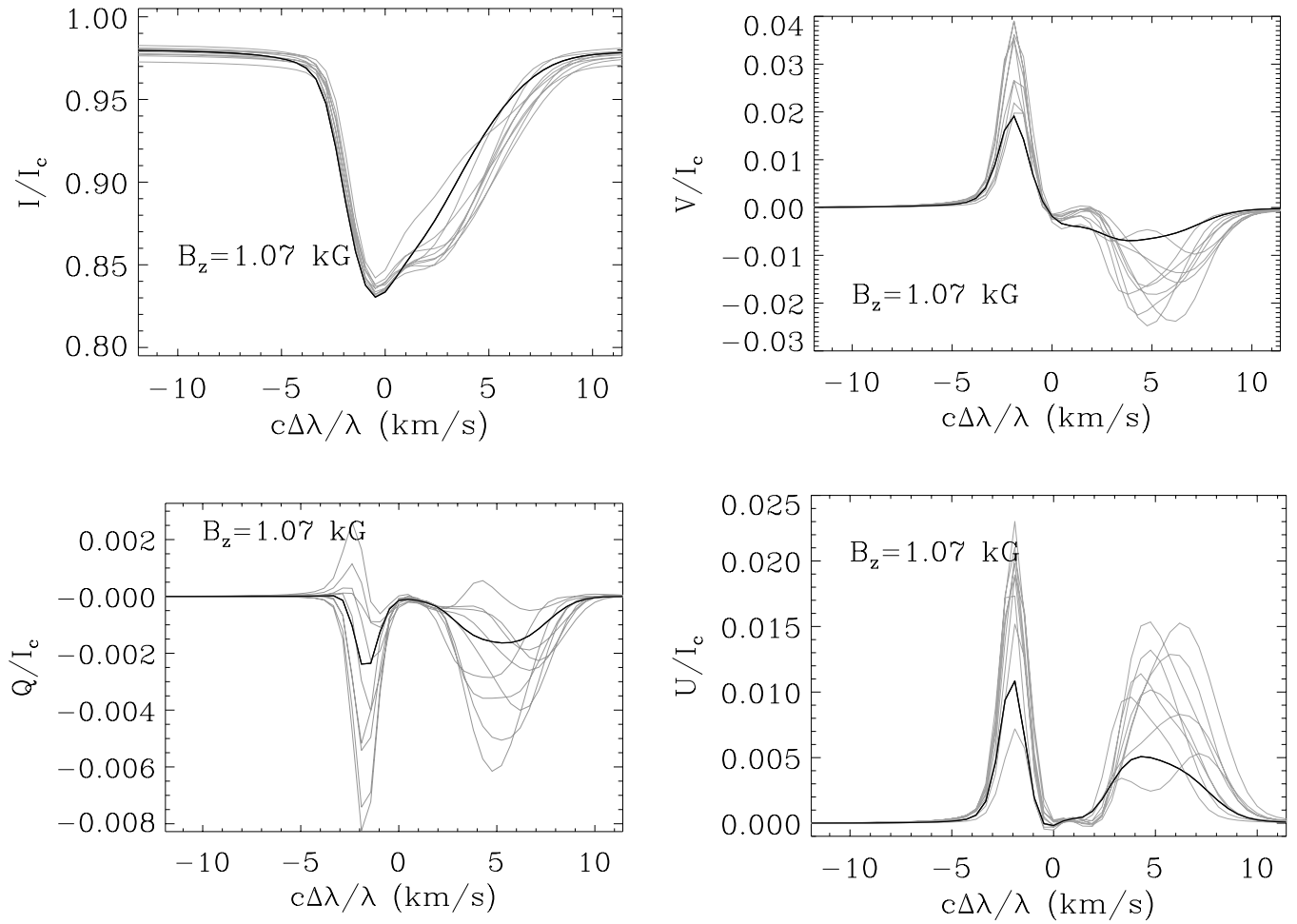
Fig. 9.—Stokes *I*, *V*, *Q*, and *U* profiles for Fe I $\lambda 6302$ as would be observed by the 97 cm Swedish Solar Telescope on La Palma with perfect seeing (*thick lines*) compared with the profiles for nine individual grid cells covering 75×75 km region around the central point (*gray lines*). The profile is degraded by the finite telescope resolution with respect to what actually occurs in the simulation.
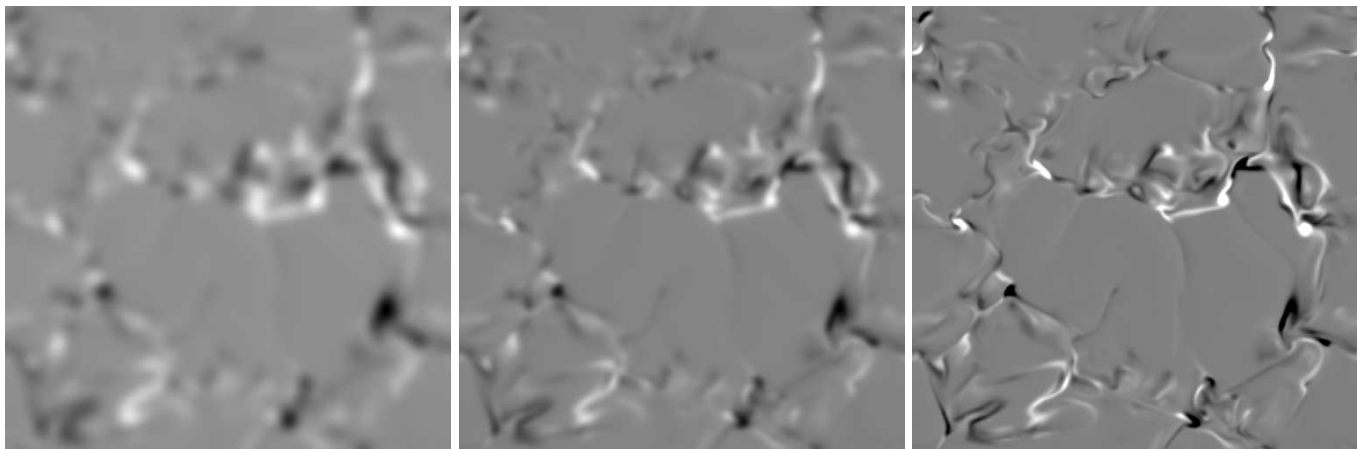

Fig. 10.—Vertical magnetic field convolved with the telescope modulation transfer function including the degradation due to seeing, which represents the Stokes *V* image as it would be observed with the old 47 cm Swedish Solar Telescope on La Palma (*left*), the new 97 cm telescope (*center*), and the image as obtained from the simulation (*right*).

APPENDIX

MAGNETIC BOUNDARY CONDITIONS

The values of all the variables at the last top and bottom layer are determined from the boundary conditions, instead of by solving the conservation equations and the induction equation. The magnetic field is calculated from the vector potential,

$$\boldsymbol{B} = \nabla \times \boldsymbol{A} + \boldsymbol{B}_0, \tag{5}$$

where $\boldsymbol{B}_0$ is a constant background field. Therefore, the boundary conditions are applied to the vector potential (rather than the magnetic field itself).

A1. TOP BOUNDARY

At the top of the domain the magnetic field is assumed to tend toward a potential field,

$$\boldsymbol{B} = \nabla \phi.$$

Since, in this case,

$$\nabla \cdot \boldsymbol{B} = \nabla^2 \phi = 0,$$

the wavevector for the Fourier components satisfies,

$$k_x^2 + k_y^2 + k_z^2 = 0. \tag{6}$$

We assume the field is decreasing at infinity. The Fourier transform in the horizontal directions (x, y) is taken of each component of the vector potential A at the vertical level, z_2, just below the boundary (after interpolating to a horizontal grid that is a power of two in each direction). Each Fourier component, $A(k_x, k_y)$, is then multiplied by $\exp(-k_z|z_2 - z_1|)$, where $k_z = (k_x^2 + k_y^2)^{1/2}$, to obtain the values of the vector potential at the boundary layer, z_1 (Deinzer et al. 1984; Hurlburt et al. 1996). The Fourier components of the vector potential at the boundary layer, z_1, are then transformed back to physical space and interpolated back to the computational grid. The effect of this boundary condition is to damp the short-wavelength components of the vector potential, leaving a more gradually varying result.

A2. BOTTOM BOUNDARY

In outflows, the boundary value of the vector potential is set from the conditions

$$\frac{\partial^2 A_x}{\partial z^2} = \frac{\partial^2 A_y}{\partial z^2} = \frac{\partial A_z}{\partial z} = 0. \tag{7}$$

This condition on the vector potential leads to the condition on $\boldsymbol{B}$ that

$$\frac{\partial B_x}{\partial z} = \frac{\partial B_y}{\partial z} = \frac{\partial^2 B_z}{\partial z^2} = 0,$$

which is consistent with the vertical derivative of $\nabla \cdot \boldsymbol{B}$ vanishing at the bottom boundary.

In inflows, a given horizontal magnetic field is advected into the computational domain. The boundary values of the vector potential are set from the conditions

$$A_x = A_z = 0, \qquad \frac{\partial A_y}{\partial z} = B_{x0}, \tag{8}$$

where B_{x0} is the imposed value of the horizontal magnetic field advected into the computational domain by the inflows at the bottom. In practice, there is a short linear ramp between inflows and outflows with a width of $1-2$ km s^{-1} in the vertical velocity. Because sharp bends in the magnetic field occur at the boundaries between in and out flows, the resistive heating of the plasma is omitted in the bottom two zones of the domain. The incoming horizontal field was set to be either $B_{x0} = 1$ or 30 G. However, checking after the fact showed that the actual field strength of the incoming horizontal field in the 30 G case was 50 G.

REFERENCES

Asplund, M., Nordlund, Å., Trampedach, R., & Stein, R. F. 2000, A&A, 359, 743
Brummell, N. H., Hurlburt, N. E., & Toomre, J. 1998, ApJ, 493, 955
Brun, A. S., Miesch, M. S., & Toomre, J. 2004, ApJ, 614, 1073
Bushby, P. J., & Houghton, S. M. 2005, MNRAS, 362, 313
Carlsson, M., Stein, R. F., Nordlund, Å., & Scharmer, G. B. 2004, ApJ, 610, L137
Cattaneo, F., Brummell, N. H., Toomre, J., Malagoli, A., & Hurlburt, N. E. 1991, ApJ, 370, 282
Cattaneo, F., Emonet, T., & Weiss, N. 2003, ApJ, 588, 1183
Cline, K. S., Brummell, N. H., & Cattaneo, F. 2003, ApJ, 599, 1449
Deinzer, W., Hensler, G., Schuessler, M., & Weisshaar, E. 1984, A&A, 139, 426
Emonet, T., & Cattaneo, F. 2001, ApJ, 560, L197
Freytag, B., Ludwig, H.-G., & Steffen, M. 1996, A&A, 313, 497
Gustafsson, B., Bell, R., Eriksson, K., & Nordlund, Å. 1975, A&A, 42, 407
Hagenaar, H. J. 2001, ApJ, 555, 448
Harvey, K. L., & White, O. R. 1999, ApJ, 515, 812
Hurlburt, N. E., Alexander, D., & Rucklidge, A. M. 2002, ApJ, 577, 993
Hurlburt, N. E., Matthews, P. C., & Proctor, M. R. E. 1996, ApJ, 457, 933
Hurlburt, N. E., & Toomre, J. 1988, ApJ, 327, 920
Hyman, J. 1979, in Advances in Computer Methods for Partial Differential Equations, ed. R. Vichnevetsky & R. S. Stepleman (New Brunswick: Int. Assoc. for Mathematics and Computers in Simulation), 313
Keller, C. U., Schüssler, M., Vögler, A., & Zakharov, V. 2004, ApJ, 607, L59
Khomenko, E. V., Martínez González, M. J., Collados, M., Vögler, A., Solanki, S. K., Ruiz Cobo, B., & Beck, C. 2005, A&A, 436, L27
Leka, K. D., & Steiner, O. 2001, ApJ, 552, 354
Lele, S. K. 1992, J. Comput. Phys., 103, 16

Magain, P. 1983, A&A, 122, 225
Nordlund, Å. 1982, A&A, 107, 1
———. 1985, Sol. Phys., 100, 209
Nordlund, Å., Brandenburg, A., Jennings, R. L., Rieutord, M., Roukolainen, J., Stein, R. F., & Tuominen, I. 1992, ApJ, 392, 647
Porter, D. H., & Woodward, P. R. 2000, ApJS, 127, 159
Rosenthal, C. S., Christensen-Dalsgaard, J., Nordlund, Å., Stein, R. F., & Trampedach, R. 1999, A&A, 351, 689
Skartlien, R., Stein, R. F., & Nordlund, Å. 2000, ApJ, 541, 468
Stein, R. F., & Nordlund, A. 1998, ApJ, 499, 914
———. 2000, Sol. Phys., 192, 91
———. 2001, ApJ, 546, 585
———. 2003, in ASP Conf. Proc. 288, Stellar Atmosphere Modeling, ed. K. W. I. Hubeny & D. Mihalas (San Francisco: ASP), 519
Steiner, O., Grossmann-Doerth, U., Knoelker, M., & Schuessler, M. 1998, ApJ, 495, 468
Tao, L., Weiss, N. O., Brownjohn, D. P., & Proctor, M. R. E. 1998, ApJ, 496, L39
Thelen, J., & Cattaneo, F. 2000, MNRAS, 315, L13
Tobias, S. M., Brummell, N. H., Clune, T. L., & Toomre, J. 1998, ApJ, 502, L177
———. 2001, ApJ, 549, 1183
Vögler, A., Shelyag, S., Schüssler, M., Cattaneo, F., Emonet, T., & Linde, T. 2005, A&A, 429, 335
Weiss, N. O., Brownjohn, D. P., Matthews, P. C., & Proctor, M. R. E. 1996, MNRAS, 283, 1153
Weiss, N. O., Proctor, M. R. E., & Brownjohn, D. P. 2002, MNRAS, 337, 293